

<https://doi.org/10.1038/s41528-025-00474-9>

Enhancing electrochemical reversibility in lithium metal batteries through structural engineering of flexible composite current collectors

Check for updates

Seungho Lee^{1,2,9}, Subi Yang^{1,2,9}, Min Sung Kang^{3,4}, Yunho Bae¹, Kyunbae Lee⁵, Yeonsu Jung⁵, Young Hyun Kim⁶, Jang-Yul Kim⁶, Kwang Chul Roh², Jihoon Seo⁷, Sung Beom Cho^{3,4}✉, Junghyun Choi⁸✉, Taehoon Kim⁵✉ & Patrick Joohyun Kim¹✉

Lithium metal batteries (LMBs) offer high energy densities but face challenges including poor reversibility and Li dendrite growth. Herein, we evaluate two flexible composite current collectors composed of reduced graphene oxide and carbon nanotubes (rGO/CNT) to investigate how Li storage mechanisms influence electrochemical performance. By modulating the number of layers in rGO, the few-layered rGO/CNT collector (FL-CC) stores Li through a pure plating mechanism, whereas the multi-layered rGO/CNT collector (ML-CC) stores lithium via a hybrid intercalation/plating mechanism. The hybrid mechanism in ML-CC promotes reversible Li-ion storage, reduces active Li-ion loss, and suppresses dendrite formation. As a result, ML-CC achieves superior cycling stability compared to FL-CC in both LMBs and anode-free LMB tests paired with LiFePO₄ cathodes at a practical areal capacity of 4.5 mAh cm⁻². This study highlights the importance of structural design in current collectors and demonstrates that incorporating lithiable materials can significantly enhance the electrochemical stability of anode-free LMBs.

Lithium-ion batteries (LIBs) are the most widely used energy-storage devices for the transportation sector and electrical devices due to their excellent electrochemical performance^{1–4}. Unfortunately, conventional LIBs face challenges in meeting the ever-growing demands for high-energy-density batteries owing to their intrinsic limits^{5–10}. Therefore, the development of new battery chemistries is essential to achieve substantial improvements in energy density. In this respect, Li-metal batteries (LMBs) have emerged as the most promising next-generation batteries owing to the lowest redox potential (−3.040 V vs. SHE) and ultrahigh theoretical specific capacity (3860 mAh g^{−1}) of a Li metal anode^{11–16}. Moreover, the pursuit of a higher energy density has led to the design of the LMBs with an anode-free configuration^{17–22}. However, the practical application of these Li-metal-based batteries is still hampered by several challenges, mainly associated

with irreversible Li plating/stripping process. Owing to host-less characteristic of metallic Li, inhomogeneous Li plating occurs and thus leads to dendritic Li during cycling, resulting in active Li-ion loss, poor coulombic efficiency (CE), and dead Li formation^{23–25}.

To address the abovementioned problems, various strategies have been proposed, including electrolyte optimization, separator modification, and introduction of three-dimensional (3D) current collectors^{26–29}. Among these strategies, the use of 3D current collectors with a large specific surface area has been demonstrated to effectively extend the cycle life of LMBs. These 3D current collectors not only provide increased Li accommodation within their internal structure compared to conventional Cu current collectors but also mitigate the substantial volume changes of Li during cycling. For instance, Zhang et al. demonstrated that a 3D-structured Cu current

¹School of Chemical Engineering and Applied Chemistry, Kyungpook National University, Daegu, Republic of Korea. ²Energy Storage Materials Center, Korea Institute of Ceramic Engineering and Technology, Jinju-si, Gyeongsangnam-do, Republic of Korea. ³Department of Materials Science and Engineering, Ajou University, Suwon-si, Gyeonggi-do, Republic of Korea. ⁴Department of Energy Systems Research, Ajou University, Suwon-si, Gyeonggi-do, Republic of Korea. ⁵Composites Research Division, Korea Institute of Materials Science (KIMS), Changwon-si, Gyeongsangnam-do, Republic of Korea. ⁶Carbon Materials Group, Research Institute of Industrial Science & Technology, Pohang-si, Gyeongsangbuk-do, Republic of Korea. ⁷Department of Chemical & Biomolecular Engineering, Clarkson University, Postdam, NY, USA. ⁸School of Chemical, Biological and Battery Engineering, Gachon University, Seongnam-si, Gyeonggi-do, Republic of Korea. ⁹These authors contributed equally: Seungho Lee, Subi Yang. ✉e-mail: csb@ajou.ac.kr; junghchoi@gachon.ac.kr; tkim67@kims.re.kr; pjkim@knu.ac.kr

collector with high porosity stabilized the Li plating process and improved the cycling stability of the LMBs³⁰. Also, Shan et al. significantly extended the cycling lifespan of Li-metal-based batteries, by utilizing a 3D Cu–carbon nanotubes (CNTs) current collector with numerous defects and pores³¹. However, the repeated Li plating and stripping on the current collector inherently induces irreversible side reactions, compromising the long-term cycling stability of LMBs. Therefore, it is of importance to design a new type of current collector with a reversible Li storage and release mechanism to achieve highly stable LMBs.

In this article, we examined two distinct flexible composite current collectors to explore the role of reversibly lithiable materials within the composite film in improving the electrochemical reversibility and cycle life of Li-metal-based batteries. The reduced graphene oxide (rGO) in the current collectors mainly acts as a Li receiver, while the CNT improves the mechanical flexibility of the carbon scaffold and prevents the restacking of rGO layers^{32–34}. By modulating the number of layers in rGOs, the rGO/CNT-based current collectors store active Li by different mechanisms: pure Li plating in the rGO/CNT current collector with few-layered rGOs (FL-CC) and a hybrid intercalation/plating mechanism in the rGO-CNT current collector with multi-layered rGOs (ML-CC). The Li-intercalated multi-layered rGO imparts lithophilicity to the ML-CC scaffold prior to Li plating, which facilitates uniform Li deposition during subsequent lithiation. As a result of the hybrid Li storage mechanism in the ML-CC, homogeneous Li plating is achieved throughout the scaffold, effectively mitigating the dendritic Li growth and dead Li formation. In contrast, the FL-CC exhibits inhomogeneous Li plating and severe dendritic Li growth. Due to these distinct Li storage mechanisms and surface affinity against Li, the ML-CC achieved excellent cycling performance over 300 cycles in LMBs. Furthermore, the ML-CC exhibited superior cycling stability in anode-free cell tests paired with an LFP cathode at a practical areal capacity (~4.5 mAh cm⁻²). This study demonstrates that the incorporation of reversibly lithiable materials into the current collector holds great potential in improving the efficiency of Li storage and release, as well as extending the cycling performances of the Li-metal-based batteries.

Results

Synthesis of GOs with varying layer counts

Figure 1a illustrates the overall fabrication process of the FL-CC and ML-CC. To synthesize the FL-CC and ML-CC, graphite is oxidized to graphite oxide with different oxidation states. The graphite oxides are then exfoliated to GOs with varying layer counts, few-layered GO and multi-layered GO. Subsequently, the obtained GOs are dispersed with single-walled CNT (SWCNT) powder in aqueous sodium dodecyl sulfate (SDS) solution by tip sonication. The SWCNTs are added to provide sufficient mechanical strength and flexibility to form freestanding film. Then, GO-CNT films are fabricated via the vacuum filtering the dispersed GO-CNT solution. After dipping each GO-CNT film in the hydrogen iodide (HI) solution, each FL-CC and ML-CC is prepared.

To synthesize the GOs with varying layer counts, graphite oxides with different oxidation states were first synthesized using the modified Hummers' method with different amounts of KMnO₄. To confirm whether the oxidation processes were successfully conducted, fourier-transform infrared spectroscopy (FT-IR) measurements were performed (Fig. S1). In the case of pristine graphite, no peak was observed except for the weak peak related to the C-C bond. However, as the oxidation state increased, the peak intensities of the oxygen-containing functional groups and the C-C bond significantly increased, indicating the successful synthesis of graphite oxides with different oxidation states³⁵. Then, the obtained graphite oxides were bath-sonicated in DI water for 24 h to synthesize GOs with varying layer counts. During the sonication process, the graphite oxides were exfoliated to GOs owing to the electrostatic repulsion force of the oxygen-containing functional groups^{36,37}. Therefore, the graphite oxides in higher oxidation states were exfoliated to few-layered GOs, whereas those in lower oxidation state were exfoliated to multi-layered GOs. To confirm if the GOs with varying layer counts are successfully synthesized, field-emission scanning electron

microscope (FE-SEM)-energy-dispersive X-ray spectroscope (EDS) and Raman analyses were performed. As presented in Fig. S2, the few-layered GOs have similar morphologies to the single-layered commercial GOs. However, it is confirmed that the morphologies of the multi-layered GOs are different from those of the few-layered GOs, which is highly likely due to the difference in the graphene layer counts (Fig. 1b, e). The corresponding EDS mapping images showed that the few-layered GOs contained considerably more oxygen atoms than the multi-layered GOs, which was in line with the FT-IR results (Fig. 1c, d, f, g). Moreover, the Raman analyses further proved that the GOs were successfully synthesized as intended (Fig. S3). As shown in Fig. S3, in the low-oxidation state, the intensity ratio of the D band (near 1350 cm⁻¹) to the G band (near 1600 cm⁻¹) (D/G ratio) increases as the oxidation level increases. However, in the high-oxidation state, the D/G ratio decreases despite the increase in the oxidation level, which is line with typical Raman spectra of the GOs in high-oxidation states. Meanwhile, the full width at half maximum of the G-band increased as the oxidation level increased, which was also highly accordant with the typical Raman results of the GOs^{35,38}. These results demonstrate that GOs with different oxidation states were synthesized.

To further investigate the number of the graphene layers of each GO, field-emission transmission electron microscope (FE-TEM) and atomic force microscope (AFM) measurements were conducted. The TEM images revealed that the exfoliated few-layered GOs were close to monolayers, while the exfoliated multi-layered GOs had multi-layered structures (Fig. 1h, k). Also, similar results were confirmed via the AFM images. In the AFM images, the difference in the height of the GOs could be distinguished by the contrast of the graphene sheets. In the case of the few-layered GOs, all the graphene sheets of few-layered GOs had similar heights of 2–3 nm, which was estimated by one or two layers of graphene sheets (Fig. 1i, j). In contrast, the multi-layered GOs have a higher number of layers in overall sheets compared to the few-layered GOs, which is in agreement with the TEM images (Fig. 1l, m). From these results, it was confirmed that the GOs with varying layer counts were successfully synthesized.

Characterization of FL-CC and ML-CC

Figure 2a, d show the Raman spectra of both GO/CNT scaffolds before and after the reduction process. As presented in the Raman spectra, the D/G ratios of both scaffolds decrease after the reduction process, which is due to the decrease in the number of oxygen atoms on the surface of the GOs³⁹. To increase the reliability of the Raman results, X-ray photoelectron spectroscopy (XPS) analyses were conducted (Fig. S4). To clearly observe the reduction effects on the GOs, the analyses were performed for pure few-layered and multi-layered GO/rGOs. Figure S4 show the deconvoluted O 1 s spectra of the GO/rGOs, confirming that oxygen-containing functional groups considerably decreased after the reduction process. These results demonstrate that the reduction processes were successfully carried out.

Figure S5 show the photographic images of both prepared current collectors, exhibiting no significant difference in appearance and excellent flexibility. This is because the mechanical flexibility is primarily depending on the ratio composition of the SWCNT. Also, both FL-CC and ML-CC were bent without a noticeable damage after galvanostatic cycling, further demonstrating their excellent flexibility. To investigate the surface morphologies of the FL-CC and ML-CC, SEM measurements were conducted. Figure 2b shows the low-magnification SEM image of the FL-CC, which reveals similar morphologies to those of the pristine CNT scaffold (Figure S6). It is likely that the uniform distribution of few-layered rGO sheets across the surface hinders the clear observation of their morphologies in low-magnification SEM image. In the high-magnification SEM image of the FL-CC, the edge of few-layered rGO was confirmed, which indicated the existence of the few-layered rGOs (Fig. 2c). However, the ML-CC showed uniformly distributed multi-layered rGOs within the CNT scaffold (Fig. 2e). The high-magnification SEM image of the ML-CC also exhibited a similar morphology, which verified the presence of the multi-layered rGOs (Fig. 2f). To increase the validity of the SEM results, Raman mapping measurements were performed. Figure 2g depicts the Raman mapping image of the pristine

CNT scaffold. It is observed that the D/G ratio of approximately 0.022 is uniformly distributed over the entire surface, which is consistent with the typical D/G ratio of SWCNTs⁴⁰. Meanwhile, the FL-CC exhibits a higher D/G ratio of approximately 0.10 that is similar value with the Fig. 2a (Fig. 2h). This further demonstrates the presence of the few-layered rGOs uniformly distributed in the scaffold. Similarly, the ML-CC shows an D/G ratio of

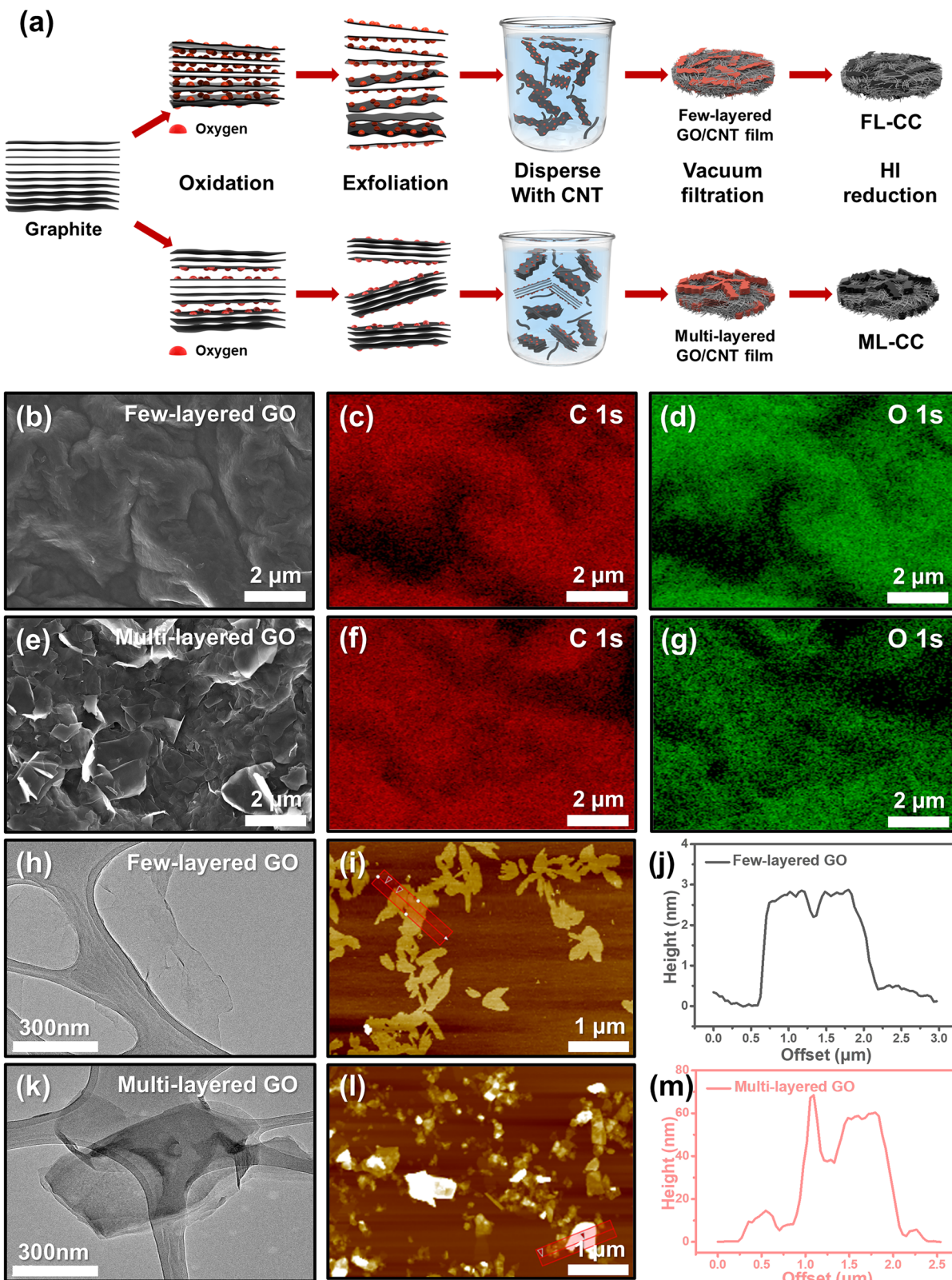


Fig. 1 | Preparation and morphology. **a** Schematic illustration for fabrication process of FL-CC and ML-CC. **b** SEM image and **c**, **d** corresponding EDS mapping images of few-layered GO. **e** SEM image and **f**, **g** corresponding EDS mapping

images of multi-layered GO. **h** TEM and **i** AFM images of few-layered GO. **j** Line profile of the red-boxed region in (i). **k** TEM and **l** AFM images of multi-layered GO. **m** Line profile of the red-boxed region in (l).

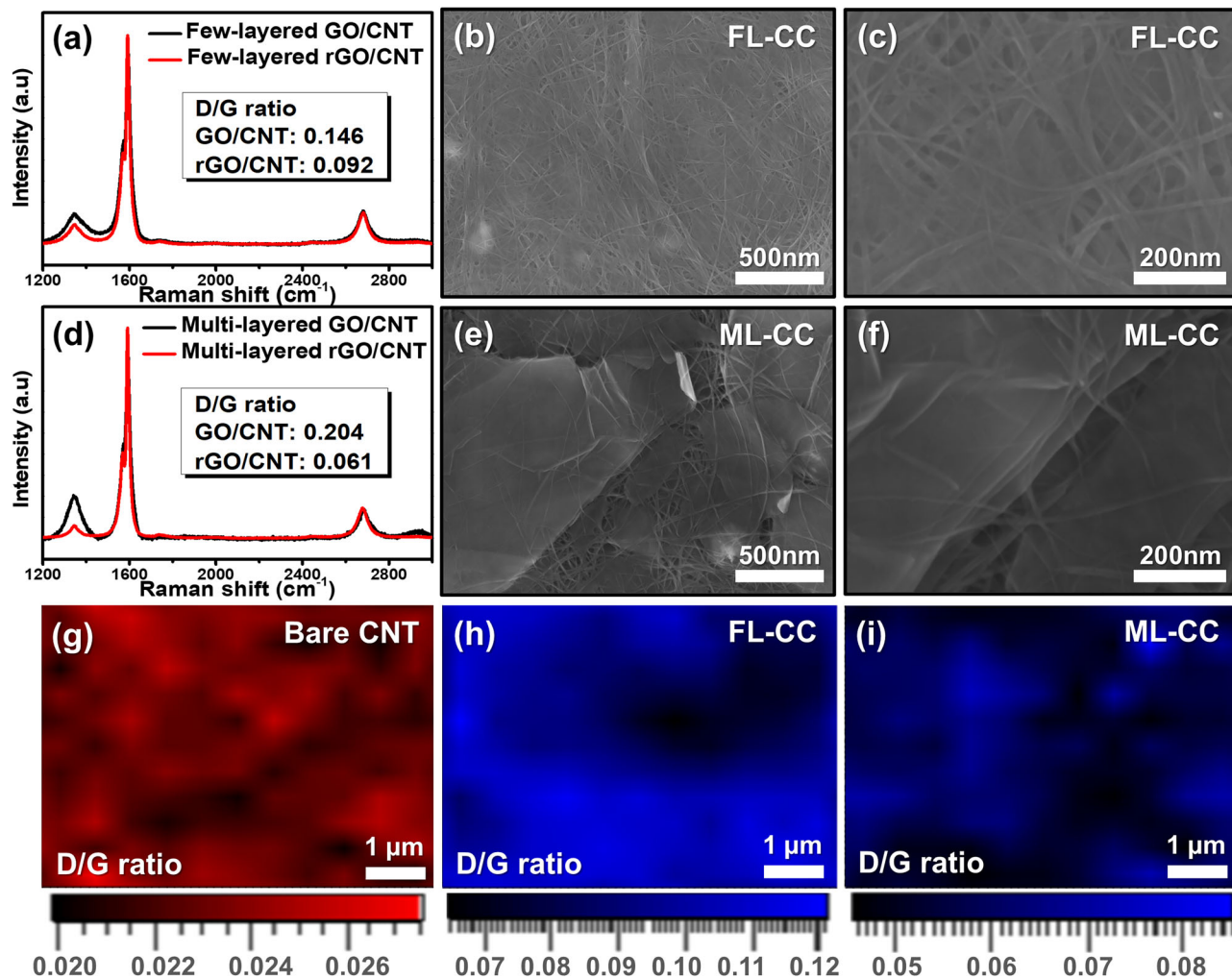


Fig. 2 | Structure. **a** Raman spectra of FL-CC before and after HI reduction process. **b** Top-view and **c** high-magnification SEM images of the FL-CC. **d** Raman spectra of ML-CC before and after HI reduction process. **e** Top-view and **f** high-magnification SEM images of ML-CC. Raman mapping images for D/G ratio of **g** bare CNT, **h** FL-CC, and **i** ML-CC.

approximately 0.06, verifying the uniform distribution of the multi-layered rGOs throughout the entire scaffold (Fig. 2i). These results confirm the successful fabrication of both scaffolds with varying rGO layer counts.

Electrochemical performances in LMB tests

To evaluate the electrochemical performances of both current collectors, Li metal cell tests were conducted. Figures 3a and S7 present the cycling performances of the Li metal cells with Cu, CNT, FL-CC, and ML-CC current collectors (i.e., Li|Cu, Li|CNT, Li|FL-CC, and Li|ML-CC cells) at a current density of 1.0 mA cm^{-2} with an areal capacity of 1.0 mAh cm^{-2} . Since the electrolyte used in the cell evaluation is the carbonate-based electrolyte without any additives, all the cells exhibit relatively poor CEs compared to the those with advanced electrolytes, which is attributed to severe parasitic reactions like continuous electrolyte decomposition and resulting accumulation of solid electrolyte interphase layer^{41–43}. In the case of the Li|Cu cell, the CE gradually decreased and significantly fluctuated after 50 cycles, which was due to the uneven Li plating and dendritic Li growth during cycling. In contrast, the Li|CNT cell showed better cycling performance than the Li|Cu cell owing to the large specific surface area of the CNT that confines excess Li, however, it suffers a significant CE fluctuation after 150 cycles due to the inevitable dendritic Li growth. Meanwhile, the Li|FL-CC cell exhibited further improvement in cycling stability compared to the Li|CNT cell. This is highly likely due to the presence of the rGO layers that are more lithiophilic than the CNT, guiding uniform Li plating during cycling^{44,45}. In addition, the Li|ML-CC cell delivered significantly improved

cycling stability and higher CEs even compared to the Li|FL-CC cell. This favorable result is attributable to the hybrid Li storage of intercalation/plating of the ML-CC. During the initial lithiation process, the Li ions preferentially intercalate into the multi-layered rGO structures due to the lower intercalation energy compared to the adsorption energy on the rGO surface, which imparts lithiophilic properties to the ML-CC (Fig. S8). Then, the Li-intercalated multi-layered rGO structures with high lithiophilicity induces uniform Li deposition during the further lithiation process, enabling reversible electrochemical reactions⁴⁶. In addition, the portion of Li stored by directly plating decreases in the ML-CC, which also contributes to achieve excellent electrochemical reversibility during cycling. However, in the case of the FL-CC with few Li-intercalatable site, the majority of Li is stored by directly plating/stripping with causing severe irreversible active Li loss, delivering poor cycling stability. When the both cells were evaluated in an elevated current density of 4.0 mA cm^{-2} , the Li|ML-CC cell maintains superior cycling performance over the Li|FL-CC cell, further validating its improved reversibility (Fig. S9).

Figure 3b presents the initial voltage profile of the Li|FL-CC and Li|ML-CC cells. In the Fig. 3b a voltage hump is observed in the Li|ML-CC cell between 0 and 0.1 V during the lithiation process, different from the Li|FL-CC cell. This voltage hump corresponds to the Li intercalation reaction in the current collector, which further verifies the occurrence of the Li intercalation into the multi-layered rGOs in the ML-CC^{47,48}. Also, similar tendency is observed in the voltage profiles at the higher current density (Fig. S9b). To further demonstrate the difference in the Li storage mechanisms of

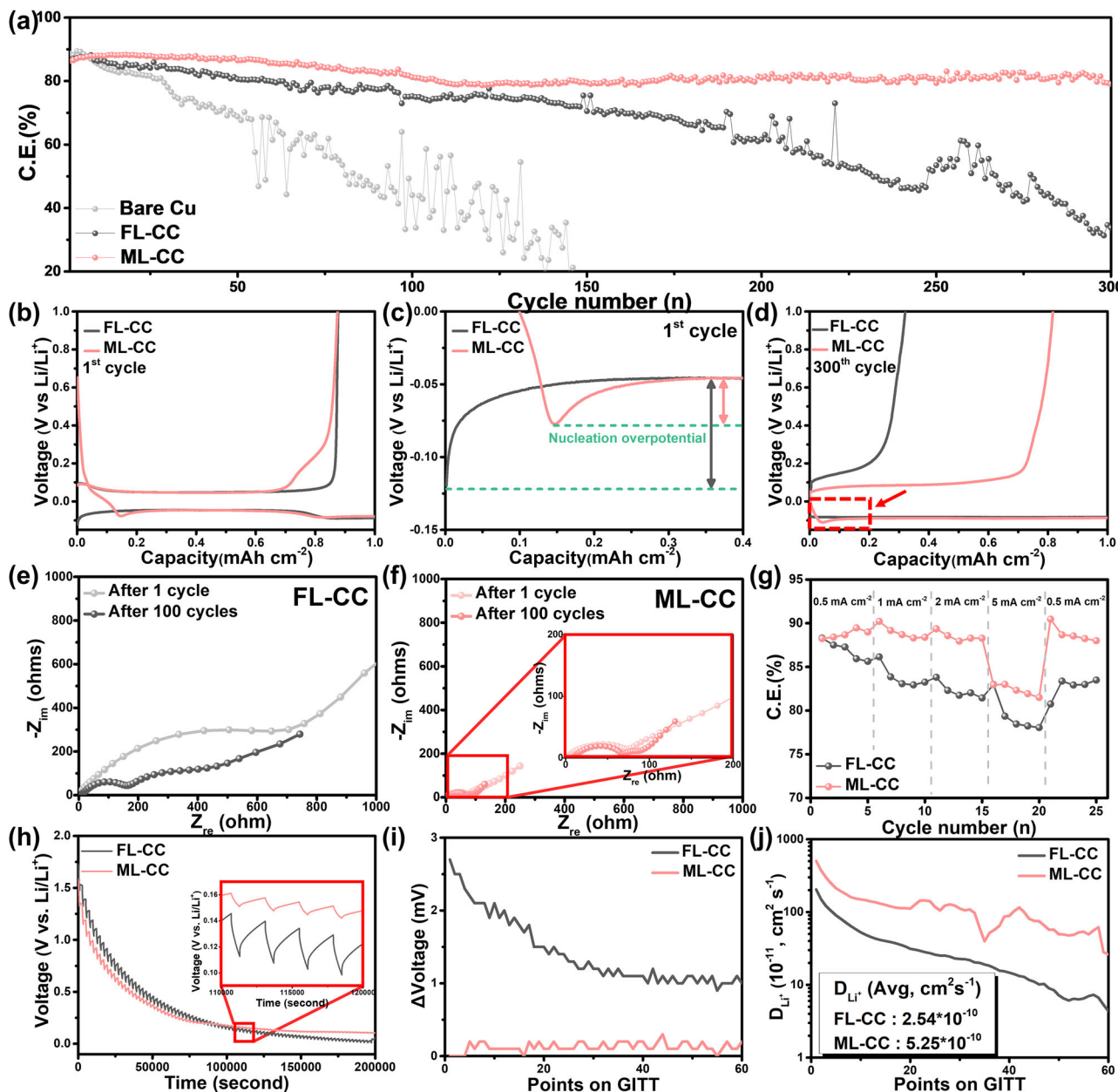


Fig. 3 | Electrochemical performance. **a** Cycling performances of Li|Cu, Li|FL-CC, and Li|ML-CC cells. Voltage profiles of Li|FL-CC and Li|ML-CC cells at the **(b, c)** initial and **d** 300th cycle. EIS Spectra of **e** Li|FL-CC and **f** Li|ML-CC cells after 1 cycle

and after cycling. **g** Rate performances of Li|FL-CC and Li|ML-CC cells at various current densities. **h** GITT curves and **i** corresponding IR drop values of Li|FL-CC and Li|ML-CC cells. **j** Li-ion diffusion coefficient values obtained from GITT tests.

each current collector, cyclic voltammetry (CV) measurements were conducted. Figure S10 shows the CV curves of each current collector after the first cycle. In contrast to the FL-CC, the ML-CC shows distinct reduction and oxidation peaks in the CV curves, which are in accordance with the typical Li intercalation/deintercalation peaks of graphite, proving that the Li intercalation/deintercalation reactions occur in the ML-CC⁴⁹. In addition, SEM analyses were performed to visually observe the intercalation reaction on the ML-CC (Fig. S11). To confirm the lithiation mechanisms of each current collector, the Li metal cells with each current collector were disassembled after Li plating at 0.2 mAh cm⁻² in the initial cycle (Fig. S11a, b). After Li plating, a Li layer was formed on the surface of the FL-CC with partially accumulated Li, compared to the SEM images before Li plating (Fig. S11c, d, g, h). However, the Li-intercalated multi-layered rGOs are observed on the ML-CC, which increases the reliability of the CV results (Fig. S11e, f, i, j). In addition, the bottom side of the ML-CC exhibits gold surface after Li plating noticeably different from the FL-CC, which is known

as the color for graphitic structures after Li intercalation, demonstrating that the Li intercalation occurs throughout the overall portion of the ML-CC (Fig. S12).

To gain deeper insight into the excellent cycling stability of the Li|ML-CC cell, nucleation overpotential of each cell was compared, which is a good indicator of the lithiophilicity of the current collector (Fig. 3c)⁵⁰. As shown in the Fig. 3c, the Li|ML-CC cell exhibits a noticeably lower nucleation overpotential (31.52 mV) than the Li|FL-CC cell (74.14 mV), revealing the high lithiophilicity of the ML-CC. This is because the lithiophilic nature of the ML-CC is ascribed to the Li-intercalated multi-layered rGO, which reduces the energy barrier for Li plating. These features result in the uniform Li plating/stripping behavior on the ML-CC, leading to excellent cycling stability. Figure S13a presents the voltage profiles of the Li|FL-CC and Li|ML-CC cells at the 150th cycle. It is confirmed that the intercalation reaction constantly occurs in the ML-CC after repetitive cycling. Also, the voltage hump is observed in the last voltage profile of the Li|ML-CC cell, indirectly

demonstrating the excellent electrochemical reversibility of the ML-CC (Fig. 3d). In addition, the Li|ML-CC cell exhibits a lower voltage hysteresis (~137 mV) than the Li|FL-CC cell (~144 mV) at the 150th cycle, increasing the reliability that the reversible electrochemical reactions occur in the ML-CC (Fig. S13b).

To further investigate the electrochemical performances, electrochemical impedance spectroscopy (EIS) analyses were conducted after 1 cycle and after cycling for the Li|FL-CC and Li|ML-CC cells (Fig. 3e, f). In the EIS spectra, the charge transfer resistance (R_{ct}) (semicircle in the higher frequency range) is a good indicator of the Li-ion reaction kinetics of the electrode. After the initial cycle, the Li|FL-CC cell exhibited an extremely high R_{ct} (~700 Ω), indirectly demonstrating the poor reaction kinetics of the FL-CC. After cycling, the R_{ct} drastically decreased to 160 Ω, which is originated from the dendritic Li growth that increases the surface area of the electrode^{51,52}. Meanwhile, the Li|ML-CC cell exhibited a constantly lower R_{ct} (~70 Ω) than the Li|FL-CC cell, even after repetitive cycling. These results indicate that the ML-CC has excellent electrochemical reversibility and superior Li-ion kinetics compared to the FL-CC owing to the hybrid Li storage mechanism and lithophilic nature. To further verify the EIS analyses, rate capability tests were performed at current densities varying from 0.5 to 5.0 mA cm⁻² (Fig. 3g). At a low current density of 0.5 mA cm⁻², the Li|ML-CC cell exhibited a slightly higher CE than the Li|FL-CC cell. However, the Li|ML-CC cell exhibited significantly higher CEs than the Li|FL-CC cell at higher current densities. Furthermore, when the current density returned to 0.5 mA cm⁻², the Li|ML-CC cell almost recovered its initial CE, while the Li|FL-CC cell delivered a decreased CE, which further demonstrates the excellent Li-ion reaction kinetics of the ML-CC.

To measure the Li-ion diffusivity of both current collectors, galvanostatic intermittent titration technique (GITT) tests were performed. Figure 3h, i present the GITT curves and the IR drop values of the cells with each current collector, respectively. Through the results, it is confirmed that the Li|ML-CC cell exhibits smaller IR drops than the Li|FL-CC cell owing to the reduced cell resistance. The Li-ion diffusion coefficient is calculated from the IR drop values using Eq. (1) (Fick's second law):

$$D_{\text{Li}^+} = \frac{4}{\pi \tau} \left(\frac{m_B V_M}{M_B S} \right)^2 \left(\frac{\Delta E_s}{\Delta E_t} \right)^2 \quad (1)$$

where τ is the titration duration, S is the surface area, m_B is the mass, M_B is the molar mass, and V_M is the molar volume of the current collector. Further, ΔE_s and ΔE_t denote the changes in voltage during the single relaxation and titration step. The average values of the D_{Li^+} for the Li|FL-CC and the Li|ML-CC cells were 2.54×10^{-10} and 5.25×10^{-10} cm² s⁻¹, respectively, which is in good agreement with the EIS and rate performance result (Fig. 3j). This result is attributed to the multi-layered rGO structures that enables hybrid Li storage mechanisms. Also, the multi-layered rGO structures have expanded interlayer spacing compared to pristine graphite due to the oxidation process of the graphite involved in the experimental process^{53,54}. The expanded interlayer spacing significantly facilitates the Li-ion diffusion into the graphitic structures, which is known as remarkably slow process than Li-ion diffusion within the graphitic structure^{55,56}. To further verify the Li-ion diffusion rate within the FL-CC and ML-CC, Tafel plot was derived from Linear Sweep Voltammetry (LSV) analysis (Fig. S14). The Tafel plot confirms that the ML-CC exhibits a higher exchange current (i_0) than the FL-CC, reflecting the rapid Li-ion transport kinetics of the ML-CC. This result increases the validity of the high D_{Li^+} of the ML-CC.

Post-mortem studies

To investigate the Li plating behavior on FL-CC and ML-CC, finite element method (FEM) simulations were conducted in conjunction with density functional theory (DFT) calculations. The calculated adsorption energies for few-layered and multi-layered rGO were -4.37 and -4.48 eV, respectively, while the intercalation energies were -5.27 and -5.90 eV, respectively, as shown in Fig. S8. These negative values indicate that both Li adsorption on the rGO surface and intercalation within

the bilayer structure are energetically favorable in both rGOs. Also, the larger magnitude of the intercalation energies compared to the adsorption energies indicates that Li ions preferentially intercalate into the bilayer structure rather than remain adsorbed on the surface. Furthermore, the results suggest that the multi-layered rGO can further enhance Li intercalation within the current collector compared to the few-layered rGO, resulting in efficient Li storage and thus uniform Li plating during cycling. These findings were clearly demonstrated in the Li plating behavior observed in the simulations, which were conducted under initial cycling conditions (Fig. 4a, h). In the simulations, the intercalation effects of Li were considered by treating each current collector as a thin layer and incorporating diffusivity within it, using the diffusion coefficient value of each current collector. Detailed specific parameters and assumptions used in the modeling are summarized in Table S1 and Experimental section. The results show the distinct Li plating behaviors between the FL-CC and ML-CC. The FL-CC exhibits uneven Li plating on its surface, which can cause the Li dendrites growth. In contrast, the ML-CC effectively suppresses inhomogeneous Li plating on its surface, which is likely due to the multi-layered rGOs within the current collector that promotes efficient Li storage during cycling. Also, the hybrid Li storage mechanism of ML-CC, which allows a greater proportion of Li to be stored within the internal structure of the current collector, results in less Li being plated on the surface compared to the FL-CC. Moreover, given the high lithophilicity of the ML-CC after initial Li intercalation, the ML-CC is expected to achieve more uniform Li plating during cycling. These results imply that integrating multi-layered rGOs within the current collector can result in uniform Li deposition and suppresses Li dendrites growth.

To further confirm the Li plating/stripping behavior on each current collector, post-mortem studies were conducted after 10 cycles. Figure S15 presents the Li plating morphologies on the Cu current collector. When the Li was plated at 0.2 mAh cm^{-2} , sharp and dendritic Li morphologies were confirmed owing to the low surface area and lithiophobic nature of the Cu current collector (Fig. S15a, d). As Li was plated further at 1.0 mAh cm^{-2} , dendritic Li growth became more severe (Fig. S15b, e). In addition, the dendritic Li remained even after Li stripping, which resulted in the dead Li formation (Fig. S15c, f). In the case of the FL-CC, relatively mossy Li plating morphologies compared to the Cu current collector were confirmed at 0.2 mAh cm^{-2} of Li plating (Fig. 4b, e). This result is due to the large specific surface area of the 3D current collector, which reduces the local current density and confines excess Li within the current collector. However, as the extent of the Li plating increases, dendritic Li morphologies were also observed on the FL-CC (Fig. 4c, f). Furthermore, after Li stripping, the dead Li was formed over the entire area of the FL-CC owing to the irreversible Li storage and release (Fig. 4d, g). Different from the FL-CC, when Li was plated on the ML-CC at 0.2 mAh cm^{-2} , smooth Li morphologies and Li-intercalated multi-layered rGOs were confirmed, which is consistent with the simulation results (Fig. 4i, l). These Li-intercalated multi-layered rGOs with high lithophilicity facilitate uniform Li plating, serving as a Li-ion redistributor that spreads the Li ions uniformly across the surface of the ML-CC^{46,57,58}. Moreover, even when the lithiation extent increases to 1.0 mAh cm^{-2} , the uniform Li plating morphologies remained with suppressing the Li dendrites growth, which is attributed to the hybrid Li storage mechanism of the ML-CC (Fig. 4j, m). Similarly, a clear surface without the dead Li formed was confirmed on the ML-CC after the Li stripping process, demonstrating that reversible storage and release occur in the ML-CC (Fig. 4k, n). To further verify the effect of the hybrid Li storage mechanism on the Li plating/stripping behavior, the Li|FL-CC and Li|ML-CC cells were disassembled after cycling. Figures S16a and S16d present the photographic images of the FL-CC and ML-CC after cycling, respectively. As illustrated in the photographic images, the cycled FL-CC exhibits an uneven surface with bumpy Li deposits, whereas the ML-CC cycle has a more uniform surface than the FL-CC. Moreover, similar results were confirmed from the SEM images of both

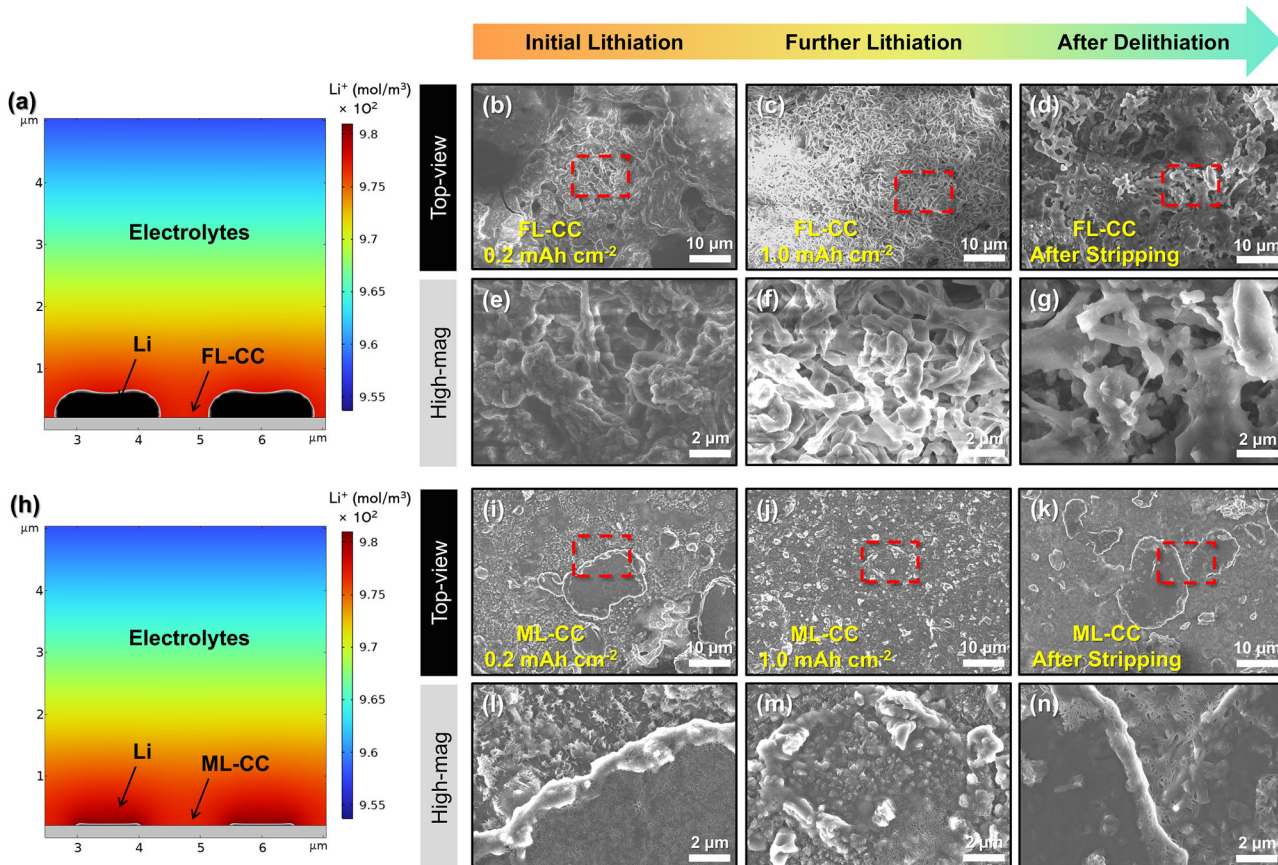


Fig. 4 | Deposition behavior. **a** Simulation result for Li plating behavior on FL-CC. Top-view SEM images of FL-CC after Li plating at **(b, e)** 0.2, **(c, f)** 1.0 mAh cm⁻², and **(d, g)** Li stripping. **(h)** Simulation result for Li plating behavior on ML-CC. Top-view SEM images of ML-CC after Li plating at **(i, l)** 0.2, **(j, m)** 1.0 mAh cm⁻², and **(k, n)** Li stripping.

cycled current collectors. Severe Li dendrites were observed on the overall surface of the cycled FL-CC, while the dendritic Li growth was noticeably suppressed on the surface of the cycled ML-CC, further proving the reversible electrochemical reactions of the ML-CC (Figs. S16b, c and S16e, f).

Electrochemical performances of FL-CC and ML-CC in anode-free LMBs

To investigate the electrochemical performances of the FL-CC and ML-CC in practical conditions, each current collector was evaluated in an LMB with anode-free condition (anode-free LMB) using an LFP cathode with a high areal capacity (~4.5 mAh cm⁻²). All the anode-free LMBs were evaluated in the carbonate-based electrolytes. Figure 5a presents the cycle performances of the anode-free LMBs with FL-CC and ML-CC (i.e., LFP | FL-CC and LFP | ML-CC cells) at a current density of 0.15 C. At the first cycle, the LFP | ML-CC cell exhibited a higher CE of 91.09% compared to the LFP | FL-CC cell (89.74%). Also, the LFP | ML-CC cell showed superior electrochemical performance (average CE of 98.09% and capacity retention of 41.33% after 50 cycles) than the LFP | FL-CC cell (average CE of 97.17% and capacity retention of 26.15% after 50 cycles) owing to the hybrid Li storage mechanism of the ML-CC. The hybrid mechanism promotes uniform deposition of the initial Li layer, leading to subsequent Li deposition more homogeneous compared to the FL-CC. Also, the uniformly deposited Li results in reduced parasitic reactions with the electrolyte and thus diminishes the active Li-ion loss during cycling, which is especially crucial for the anode-free LMBs with limited Li sources. Figure S17a, b display the voltage profiles of the LFP | FL-CC and LFP | ML-CC cells. As shown in the voltage profiles, the LFP | FL-CC cell suffered a rapid capacity decay upon cycling, when compared to the LFP | ML-CC cell. Moreover, the LFP | ML-CC cell exhibited much lower voltage hysteresis than the LFP | FL-CC cell, further

demonstrating the excellent electrochemical reversibility of the hybrid Li storage mechanisms (Fig. S17c).

Typically, the irreversible active Li-ion loss caused by side reactions at the initial cycles is one of the main reasons for the rapid capacity decay of the anode-free LMBs. In order to compare the cycling stability of the anode-free LMBs using each current collector with reduced side reactions and stabilized surface, pre-activation processes were conducted before the cell fabrication⁵⁹. For the pre-activation processes, the cells were cycled at a low current density with multiple cycles²¹. After the activation process, the LFP | ML-CC delivered excellent cycling performance of a capacity retention of over 80% after 50 cycles with an average CE of 99.15%, which is more stable than that of the LFP | FL-CC cell (capacity retention of 71.5% and average CE of 98.92%) (Fig. S18). Likewise, similar results were obtained when each cell was evaluated under a harsher test condition of 0.3 C (Fig. 5b–d). Even after the activation process, the LFP | FL-CC cell suffered a rapid capacity decay from 20 cycles with fluctuating CEs. This is attributed to the irreversible Li storage/release of the FL-CC, which results in the dead Li formation and active Li-ion loss during cycling. However, the LFP | ML-CC cell retained a stable cycling performance even at the high current density, further highlighting the excellent electrochemical reversibility of the hybrid Li storage mechanism. In conclusion, these results demonstrate that the electrochemical performances of the anode-free LMBs can be significantly improved by incorporating reversibly lithiable materials into the current collectors.

To validate that ML-CC maintains consistent performance under mechanical deformation, cycling stability of anode-free LMBs employing the ML-CC before and after multiple bending cycles was compared (Fig. 5e). The ML-CC exhibited nearly identical CE and capacity retention in both cases, demonstrating its structural flexibility and mechanical reliability. To further demonstrate the mechanical flexibility of ML-CC as a current

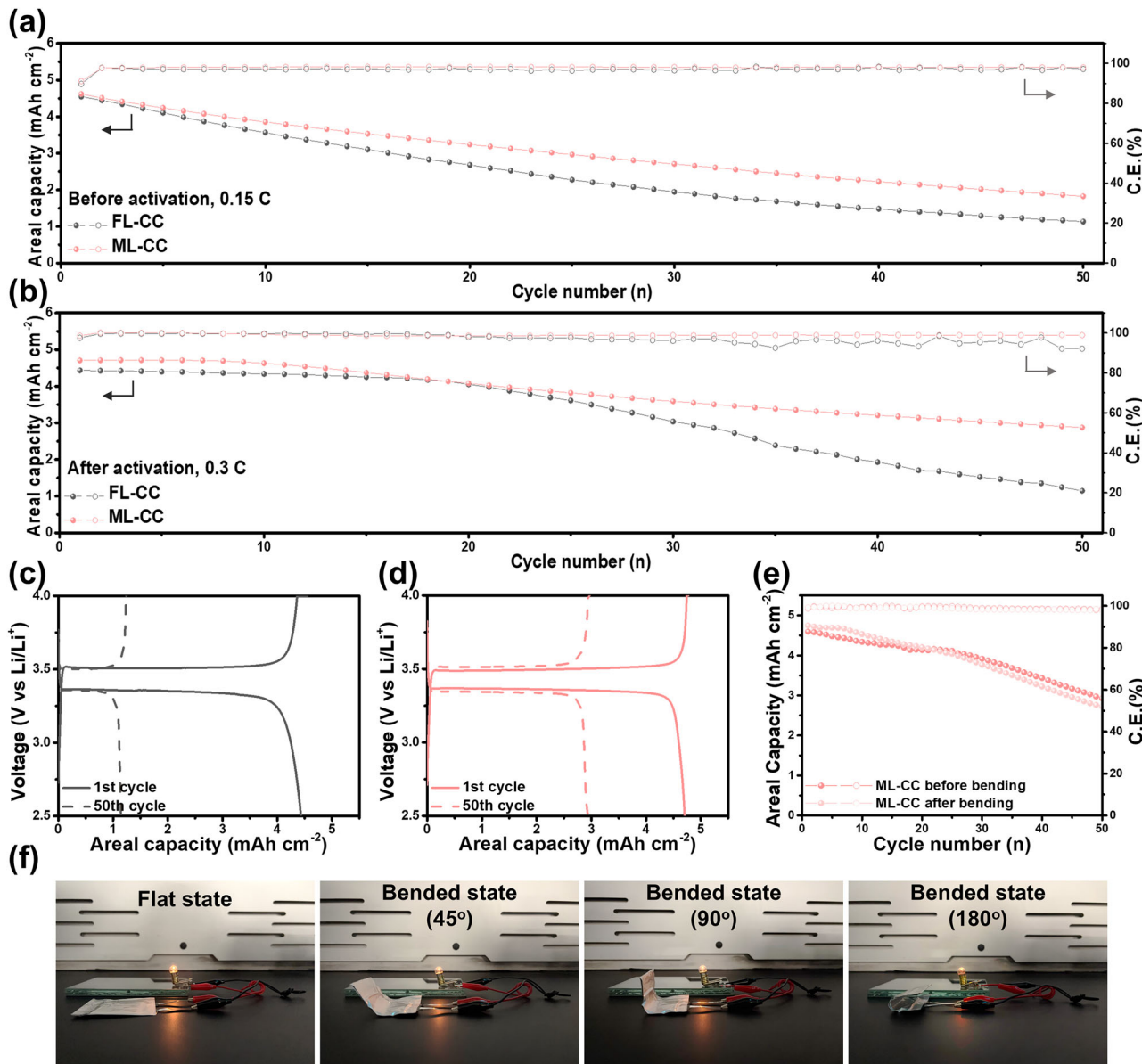


Fig. 5 | Electrochemical performances of FL-CC and ML-CC in anode-free LMB tests upon pairing with LFP cathode with a practical areal capacity (~4.5 mAh cm⁻²).

a Cycling performances of LFP | FL-CC and LFP | ML-CC cells at 0.15 C before activation process. **b** Cycling performances of LFP | FL-CC and LFP | ML-CC cells at 0.3 C after activation process. Voltage profiles of **c** LFP | FL-CC

and d LFP | ML-CC after activation process for the initial and final cycle. **e** Cycling performances of ML-CC before and after bending in anode-free LMB.

f Photographic images of pouch cell with ML-CC, powering a lightbulb under various bending conditions (flat, 45°, 90°, and 180°).

collector, pouch-type cells were fabricated and evaluated under various mechanical deformation states. The cells were connected to a lightbulb and tested in the flat state as well as after being bent to 45°, 90°, and 180°. In all cases, the lightbulb operated successfully, confirming the stable electrical performance of the ML-CC (Fig. 5f). Moreover, voltage profiles obtained from galvanostatic cycling before and after bending were nearly identical, further supporting the mechanical durability of the ML-CC as the current collector (Fig. S19).

Figure 6 illustrates how the incorporation of reversibly lithiable materials within the current collector enhances the electrochemical reversibility of Li storage and release processes in Li-metal-based batteries. In the FL-CC, Li ions are directly plated onto the surface rather than being intercalated into the carbon structure of the current collector. This leads to the formation of inhomogeneous Li nuclei, which further promotes severe dendritic Li growth during charging. The formation of dendritic Li on the surface of the FL-CC not only elevates the risk of internal short circuits but

also contributes to rapid capacity fading due to the accelerated loss of active Li. In contrast, the ML-CC incorporating reversibly lithiable materials, the multi-layered rGO, allows for Li-intercalation during the initial stage of lithiation. This Li-intercalation process imparts lithiophilic properties to the backbone of the ML-CC, enhancing its surface affinity for Li ions. As a result, Li ions are more uniformly distributed within the current collector, promoting uniform Li plating during subsequent charging cycles. Then, the dendritic Li growth and formation of dead Li on the ML-CC is effectively suppressed. Consequently, the ML-CC achieves a highly reversible Li storage and release process, leading to excellent cycling stability. The improved performance of the ML-CC highlights the importance of incorporating reversibly lithiable materials within the current collector.

Discussion

In this study, we assessed two different flexible rGO/CNT current collectors to correlate Li storage mechanisms with the electrochemical performance of

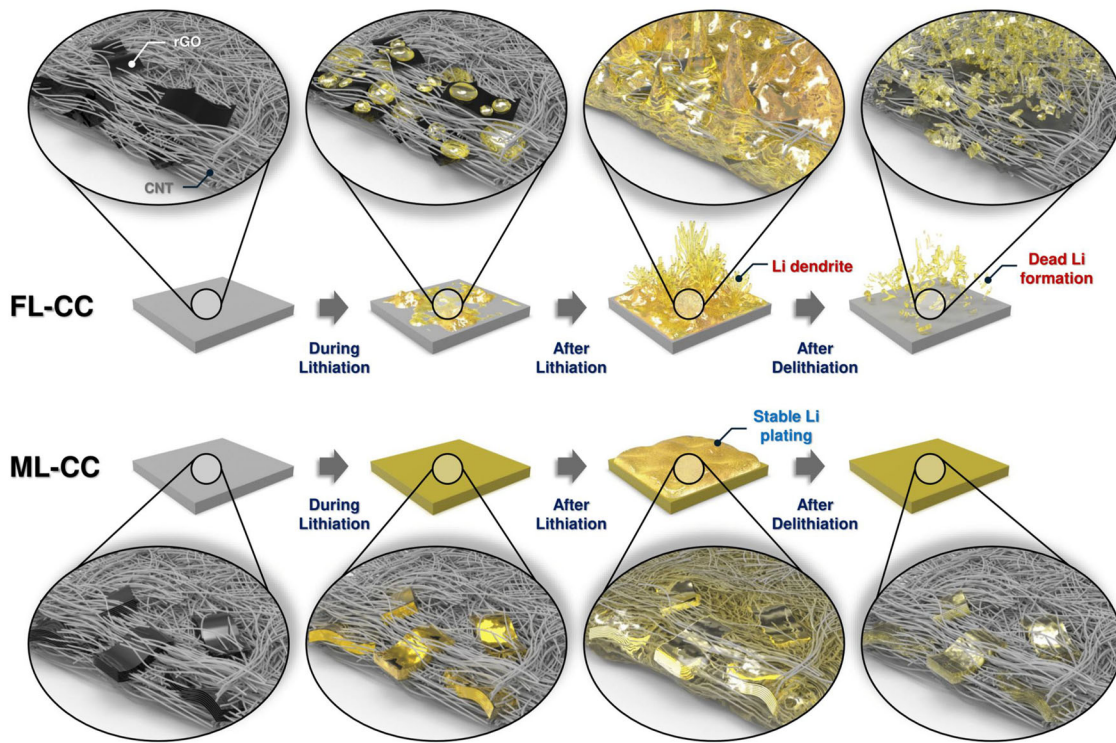


Fig. 6 | Schematic illustration to explain the roles of reversibly lithiable materials within the scaffold on Li plating/stripping behavior on FL-CC and ML-CC.

Li-metal-based batteries. By modulating the number of layers in rGO, each current collector exhibits a distinct Li storage mechanism: pure plating in the FL-CC with few-layered rGO and hybrid intercalation/plating in the ML-CC with multi-layered rGO. When both current collectors were evaluated in LMB tests, the ML-CC exhibited significantly improved cycling stability compared to the FL-CC, suppressing dendritic Li growth and dead Li formation. These favorable results are attributed to the hybrid Li storage mechanism of the ML-CC. During the initial lithiation process, Li-ions are stored in the ML-CC via intercalation, which imparts lithophilic properties to the backbone of the ML-CC, facilitating uniform Li plating throughout the scaffold and suppressing dendritic Li growth during subsequent lithiation processes. As a result, when the current collectors were evaluated in LMB tests including anode-free LMB with a practical areal capacity of 4.5 mAh cm^{-2} , the ML-CC exhibited superior cycling performance compared to the FL-CC. Considering these results, it is confirmed that incorporating reversibly lithiable materials into the fabrication of current collectors significantly enhances electrochemical stability and cycle performance in Li-metal-based batteries including anode-free LMBs. This study provides new insights into the rational design of carbon-based current collectors and would serve as a valuable guide for designing next-generation current collectors for practical Li-metal-based batteries.

Methods

Synthesis of GOs with varying layer counts

To fabricate FL-CC and ML-CC, GOs with varying layer counts were synthesized. The GOs were synthesized using modified Hummers' method^{3,5,60}. First, graphite flake (2 g, 99%, natural, Sigma Aldrich) was stirred in H_2SO_4 (60 ml, 95%, Duksan) in a water bath at 50 °C. Subsequently, KMnO_4 powder ($\geq 99.0\%$, Sigma-Aldrich) was slowly added to the solution (10–15 g for FL-CC and 0.5–1 g for ML-CC). After 3 h stirring, the resulting solution was diluted with DI water (600 ml) and stirred for additional 15 min. Then, H_2O_2 solution (40 ml, 30.0–35.5%, Samchun) was added to the solution and further stirred for 24 h. After stirring, the resulting graphite oxide solution was washed with a HCl solution (0.01 N) for 3 times and DI water until the pH reached 7. After the washing, the centrifuged solution was sonicated for 2 days to exfoliate the graphite oxides into GOs.

Preparation of FL-CC and ML-CC

GO (3.75 mg) and SWCNT powder (1.25 mg) were added into SDS DI solution (0.5 wt%) and dispersed by tip sonication for 90 min. Then, the dispersed solution was vacuum-filtered on a mixed cellulose ester membrane (0.2 μm). To remove the SDS residue, the filtered film was subsequently washed with DI water (300 ml) and dried in the convection oven set at 50 °C. After drying, the GO/CNT film was stripped from the membrane and dipped in HI solution (57%, Sigma-Aldrich) for 5 min to reduce the GO/CNT to rGO/CNT film (FL-CC and ML-CC)⁶¹. The thickness and the mass density of the FL-CC and ML-CC is $4.38 \pm 0.85 \mu\text{m}$ (StDev), $8.29 \pm 1.54 \mu\text{m}$ (StDev) and $1.047, 0.642 \text{ g/cm}^3$, respectively. The electrical conductivity of the FL-CC and the ML-CC is 0.338 and 0.266 S/cm, respectively.

Characterizations

To confirm the oxidation states of graphite oxides, FT-IR was performed with a FT-IR spectrometer (IRXross, Shimadzu). A FE-TEM (Titan G2 ChemiSTEM Cs Probe, FEI company) and an AFM (NX20, Park systems) were used to investigate the microstructures of GOs with varying layer counts. The morphologies and post-mortem images of GO, FL-CC, and ML-CC were observed using FE-SEM (SU8230, Hitachi), along with corresponding EDS (Ultim Max100, OXFORD). To observe the surface morphology of plated Li, the cells were disassembled and subsequently washed with diethyl carbonate (DEC) to remove residual Li salts. The Raman spectra and Raman mapping images were obtained using a Raman spectrometer (inVia reflex, Renishaw). The XPS analyses were carried out with an XPS spectrometer (ThermoFisher, NEXSA). The electrical conductivity was measured using a 4-point probe method (CESH-e, Biologic).

Electrochemical measurements

Li metal cell tests for each current collector were performed with a 16 mm diameter of 1.0 T Li metal foil using CR2032 type coin cells. All the Li metal cells were assembled with 1.0 M LiPF_6 in EC/DEC (volume ratio of 1:1) using PP separators (Celgard 2400) in an argon-filled glove box. Anode-free cells were assembled with 1.15 M LiPF_6 in EC/EMC/DEC (volume ratio of 2/4/4) (with 10 wt% FEC, 1 wt% LiPO_2F_2 , and 1 wt% VC), paired with an

LFP cathode. The current collectors were punched into 12 mm and 14 mm diameter discs for the Li metal and anode-free cell tests, respectively. For the Li metal cells, repetitive Li plating/stripping tests were performed with a 1.0 V (vs. Li/Li⁺) cut-off potential for Li stripping using a battery tester (CT-4008Q-5V100mA-124, Neware). Anode-free cell tests were evaluated in a voltage range between 2.5 and 4.0 V. To measure the cell impedance, EIS (VSP-300, Biologic) was tested in the frequency ranging from 200 kHz to 10 mHz. The CV tests were conducted with a voltage window of 0–1 V at a scan rate of 0.1 mV using the Biologic instrument. To measure the Li-ion diffusion coefficients of each current collector, GITT tests were performed in the voltage window of 0.01–2.0 V with a series of pulse current (0.005 mA cm⁻² for 10 min), followed by a relaxation step for 30 min. To achieve Tafel plot, LSV analyses were conducted in the voltage range of –0.2–0.2 V with a scan rate of 0.05 mV/s.

DFT calculation

Density functional theory (DFT) calculations were performed using the VASP package and the projector augmented wave (PAW) potentials^{62,63}. The Perdew–Burke–Ernzerhof exchange-correlation functional was used to assess the precision of the implementation⁶⁴. The electronic wave functions were expanded in plane waves with a cutoff energy of 520 eV to minimize the Pulay stress during the structural optimization. The structural optimization was truncated when the Hellmann–Feynman forces reached the threshold value of 0.01 eV/Å. A Γ -centered k -points mesh of $3 \times 3 \times 1$ was employed to sample the two-dimensional Brillouin zone. The adsorption energy (ΔE_{ads}) and the intercalation energy (ΔE_{int}) were calculated by following equation:

$$\Delta E_{\text{ads/int}} = E_{\text{Total}}^{\text{ads/int}} - (E_{\text{rGO}} + E_{\text{Li}}) \quad (2)$$

where, E_{Total} was the total energy of the system, E_{rGO} was the total energy of layered rGO, and E_{Li} was the total energy of the isolated Li atom.

FEM simulation

The finite element method (FEM) simulation was employed to investigate the Li behavior in the Li|Cu asymmetric cell. The deposition modeling was carried out using COMSOL Multiphysics 6.2 software. The model incorporates three types of physics: electrochemistry, ion transport and level set to simulate the Li deposition behavior on the electrode. Electrochemical parameters such as diffusion coefficients, exchange current density and external potential were set based on experimental Li metal cell tests.

The transport of diluted species i in an electrolyte is governed by the following mass balance equation:

$$\frac{\partial c_i}{\partial t} + \nabla \cdot J_i = 0 \quad (3)$$

where J_i is the flux of species i . The flux is described by the Nernst–Planck equation, which accounts for the effects of diffusion, convection, and migration of charged species. In this model, we considered the transport of charged ions through both diffusion and migration. Thus, the ionic flux can be expressed as:

$$J_i = -D_i \nabla c_i - \frac{D_i z_i F}{k_B T} c_i \nabla \phi \quad (4)$$

where D_i is the diffusion coefficient of i , c_i is the concentration of an ionic species i , z_i is the valence charge, F is the Faraday constant, k_B is the Boltzmann constant, and ϕ is the electrolyte potential, which was set to 1.0 V. The first and second terms on the right-hand side of the equation represent diffusion driven by the concentration gradient and electromigration due to the electric field, respectively.

Electrochemical analysis was performed using the secondary current distribution method, which accounts for concentration gradients and electrode kinetics. Charge transport within the electrolyte was described

using Ohm's law:

$$i_l = -\sigma_l \nabla \phi \quad (5)$$

and the continuity equation for the current density:

$$\nabla \cdot i_l = 0 \quad (6)$$

Where i_l is the current density vector and σ_l is the electrical conductivity of the electrolyte. To maintain periodic boundary conditions, the lateral boundaries of the system were set with zero electric flux:

$$-\mathbf{n} \cdot \mathbf{i}_l = 0 \quad (7)$$

Where \mathbf{n} is the normal vector to the boundary. The local current density at the electrode surface and the overpotential were modeled using concentration-dependent kinetics described by the Butler–Volmer equation:

$$i_{\text{loc}} = i_o \left[c_R \exp\left(\frac{\alpha_a F \eta}{RT}\right) - c_O \exp\left(\frac{\alpha_c F \eta}{RT}\right) \right] \quad (8)$$

where i_{loc} is the local charge transfer current density, i_o is the exchange current density, which was set to 1.0 mA cm⁻². c_R and c_O are the concentration of reduced and oxidized species, respectively, η is the overpotential, R is the gas constant, α_a and α_c are the charge transfer coefficients of the anodic and cathodic, respectively.

The level set method was integrated to precisely model the dynamic interface evolution during lithium electrodeposition.

A scalar level set variable (ϕ), ranging from 0 (deposited lithium metal) to 1 (electrolyte), distinguishes between the two domains, with the interface represented by the contour line at $\phi = 0.5$. The evolution of the level set variable is governed by:

$$\frac{\partial \phi}{\partial t} + u \cdot \nabla \phi = \gamma \nabla \cdot \left(\epsilon \nabla \phi - \phi(1-\phi) \frac{\nabla \phi}{|\nabla \phi|} \right) \quad (9)$$

Where ϵ is the interface thickness and is defined as $\epsilon = h_{\text{max}}/4$ with h_{max} representing the maximum mesh element size. The reinitialization parameter γ is selected based on the maximum velocity magnitude observed in simulations.

The level set delta function is approximated by:

$$\delta = 6|\phi(1-\phi)||\nabla \phi| \quad (10)$$

The interface velocity u , which drives the movement of the deposition interface, was derived from the local lithium deposition current density i_{loc} according to:

$$u = n \frac{i_{\text{loc}} M_{\text{Li}}}{F \rho_{\text{Li}}} \quad (11)$$

Where the interface normal vector n is calculated as:

$$n = \frac{\nabla \phi}{|\nabla \phi|} \quad (12)$$

Boundary conditions for the level set variable were specified to accurately represent physical inlet and outlet flux conditions, ensuring the realistic modeling of Li deposition phenomena.

Data availability

Data is provided within the manuscript or supplementary information files.

Received: 19 May 2025; Accepted: 15 August 2025;
Published online: 24 September 2025

References

- Lu, J., Wu, T. & Amine, K. State-of-the-art characterization techniques for advanced lithium-ion batteries. *Nat. Energy* **2**, 17011 (2017).
- Jung, S.-K. et al. Lithium-free transition metal monoxides for positive electrodes in lithium-ion batteries. *Nat. Energy* **2**, 16208 (2017).
- Choi, J. W. & Aurbach, D. Promise and reality of post-lithium-ion batteries with high energy densities. *Nat. Rev. Mater.* **1**, 16013 (2016).
- Lin, L. et al. Adjustable mixed conductive interphase for dendrite-free lithium metal batteries. *ACS Nano* **16**, 13101–13110 (2022).
- Tikekar, M. D., Choudhury, S., Tu, Z. & Archer, L. A. Design principles for electrolytes and interfaces for stable lithium-metal batteries. *Nat. Energy* **1**, 16114 (2016).
- Ding, P. et al. Polymer electrolytes and interfaces in solid-state lithium metal batteries. *Mater. Today* **51**, 449–474 (2021).
- Lee, S. et al. Dendrite-suppressed Li deposition enabled by surface-tailored carbon-based current collectors for high-rate and stable Li-metal batteries. *Carbon* **221**, 118941 (2024).
- Yang, S. et al. Uniform Li deposition through the graphene-based ion-flux regulator for high-rate Li metal batteries. *ACS Appl. Mater. Interfaces* **16**, 3416–3426 (2024).
- Liu, H. et al. A novel design of 3D carbon host for stable lithium metal anode. *Carbon Energy* **4**, 654–664 (2022).
- Wang, J., Wang, K. & Xu, Y. Emerging two-dimensional covalent and coordination polymers for stable lithium metal batteries: from liquid to solid. *ACS Nano* **15**, 19026–19053 (2021).
- Liu, J. et al. Pathways for practical high-energy long-cycling lithium metal batteries. *Nat. Energy* **4**, 180–186 (2019).
- Stoltz, L., Homann, G., Winter, M. & Kasnatscheew, J. The Sand equation and its enormous practical relevance for solid-state lithium metal batteries. *Mater. Today* **44**, 9–14 (2021).
- Wang, J. et al. Challenges and progresses of lithium-metal batteries. *Chem. Eng. J.* **420**, 129739 (2021).
- Zhang, Y. et al. Reactivating the dead lithium by redox shuttle to promote the efficient utilization of lithium for anode free lithium metal batteries. *Adv. Funct. Mater.* **33**, 2301332 (2023).
- Chen, J. et al. Engineering high-performance Li metal batteries through dual-gradient porous Cu-CuZn Host. *ACS Nano* **18**, 13662–13674 (2024).
- Ha, S., Hyun, J. C., Kwak, J. H., Lim, H.-D. & Yun, Y. S. Hierarchically nanoporous 3D assembly composed of functionalized onion-like graphitic carbon nanospheres for anode-minimized Li metal batteries. *Small* **16**, 2003918 (2020).
- Wu, Y. et al. Multifunctional lithium compensation agent based on carbon edges catalysis and its application in anode-free lithium batteries. *Chem. Eng. J.* **458**, 141411 (2023).
- Lin, L. et al. Li-Rich $\text{Li}_2[\text{Ni}0.8\text{Co}0.1\text{Mn}0.1]\text{O}_2$ for anode-free lithium metal batteries. *Angew. Chem. Int. Ed.* **60**, 8289–8296 (2021).
- Lohrberg, O. et al. Benchmarking and critical design considerations of zero-excess Li-metal batteries. *Adv. Funct. Mater.* **33**, 2214891 (2023).
- Pyo, S. et al. Lithiophilic wetting agent inducing interfacial fluorination for long-lifespan anode-free lithium metal batteries. *Adv. Energy Mater.* **13**, 2203573 (2023).
- Kim, J., Lee, G. R., Chung, R. B. K., Kim, P. J. & Choi, J. Homogeneous Li deposition guided by ultra-thin lithiophilic layer for highly stable anode-free batteries. *Energy Storage Mater.* **61**, 102899 (2023).
- Qian, L. et al. Advanced material engineering to tailor nucleation and growth towards uniform deposition for anode-less lithium metal batteries. *Small* **18**, 2205233 (2022).
- Kim, S., Lee, M., Oh, S. & Ryu, W.-H. Li-Dendrite cage electrode with 3-D interconnected pores for Anode-Free Lithium-Metal batteries. *Chem. Eng. J.* **474**, 145447 (2023).
- Wu, W. et al. Ultralight lithiophilic three-dimensional lithium host for stable high-energy-density anode-free lithium metal batteries. *Energy Storage Mater.* **63**, 102974 (2023).
- Schöner, S. et al. Chemical prelithiated 3D Lithiophilic-/Phobic interlayer enables long-term Li Plating/Stripping. *ACS Nano* **18**, 17924–17938 (2024).
- Kim, J., Choi, J. & Kim, P. J. A new approach to stabilize the electrochemical performance of Li metal batteries through the structure alteration of CNT scaffolds. *Carbon* **203**, 426–435 (2023).
- Zhu, Y., Wu, S., Zhang, L., Zhang, B. & Liao, B. Lithiophilic ZnN_2 -modified Cu current collectors by a novel FCVA technology for stable anode-free lithium metal batteries. *ACS Appl. Mater. Interfaces* **15**, 43145–43158 (2023).
- Natarajan, K. et al. Tuning intrinsic lithiophilicity of copper foil to improve electrochemical performance of anode-free Li metal battery. *J. Energy Storage* **84**, 110880 (2024).
- Liu, W. et al. Lithiophilic Sn layer via pre-electroplating to realize the uniform stripping/plating for dendrite free Li metal anodes. *Chem. Eng. J.* **475**, 146153 (2023).
- Zhang, S. et al. Ultrathin hierarchical porous Cu current collector fabricated by anodic oxidation in complexing agent system for stable anode-free Lithium metal batteries. *Electrochim. Acta* **442**, 141895 (2023).
- Shan, C. et al. Cu-CNTs current collector fabricated by deformation-driven metallurgy for anode-free Li metal batteries. *Carbon* **204**, 367–376 (2023).
- Hu, Z. et al. Lithiophilic carbon nanofiber/graphene nanosheet composite scaffold prepared by a scalable and controllable biofabrication method for ultrastable dendrite-free lithium-metal anodes. *Small* **18**, 2104735 (2022).
- Chang, J., Huang, Q., Gao, Y. & Zheng, Z. Pathways of developing high-energy-density flexible lithium batteries. *Adv. Mater.* **33**, 2004419 (2021).
- Zhang, Y. -j et al. Integrated reduced graphene oxide multilayer/Li composite anode for rechargeable lithium metal batteries. *RSC Adv.* **6**, 11657–11664 (2016).
- Krishnamoorthy, K., Veerapandian, M., Yun, K. & Kim, S. J. The chemical and structural analysis of graphene oxide with different degrees of oxidation. *Carbon* **53**, 38–49 (2013).
- Brisebois, P. P. & Siaj, M. Harvesting graphene oxide – years 1859 to 2019: a review of its structure, synthesis, properties and exfoliation. *J. Mater. Chem. C* **8**, 1517–1547 (2020).
- Park, S. et al. Colloidal suspensions of highly reduced graphene oxide in a wide variety of organic solvents. *Nano Lett.* **9**, 1593–1597 (2009).
- Muzyka, R., Drewniak, S., Pustelný, T., Chrubasik, M. & Gryglewicz, G. Characterization of graphite oxide and reduced graphene oxide obtained from different graphite precursors and oxidized by different methods using raman spectroscopy. *Materials* **11**, 1050 (2018).
- Hu, Y., Song, S. & Lopez-Valdivieso, A. Effects of oxidation on the defect of reduced graphene oxides in graphene preparation. *J. Colloid Interface Sci.* **450**, 68–73 (2015).
- Kumar, M. & Ando, Y. Single-wall and multi-wall carbon nanotubes from camphor—a botanical hydrocarbon. *Diam. Relat. Mater.* **12**, 1845–1850 (2003).
- Liu, S. et al. An inorganic-rich solid electrolyte interphase for advanced lithium-metal batteries in carbonate electrolytes. *Angew. Chem. Int. Ed.* **60**, 3661–3671 (2021).
- Yeddala, M., Ryneison, L. & Lucht, B. L. Modification of carbonate electrolytes for lithium metal electrodes. *ACS Energy Lett.* **8**, 4782–4793 (2023).
- Ren, Q. et al. Inorganic/organic composite fluorinated interphase layers for stabilizing ether-based electrolyte in high-voltage lithium metal batteries. *J. Mater. Chem. A* **12**, 1072–1080 (2024).

44. Wang, Q. et al. Ultrathin composite Li electrode for high-performance Li metal batteries: a review from synthetic chemistry. *Adv. Funct. Mater.* **33**, 2213648 (2023).
45. Yan, X. et al. Multifunctional roles of carbon-based hosts for Li-metal anodes: a review. *Carbon Energy* **3**, 303–329 (2021).
46. Duan, J. et al. Is graphite lithiophobic or lithiophilic?. *Natl Sci. Rev.* **7**, 1208–1217 (2020).
47. Ma, X. et al. Exfoliated multi-layered graphene anode with the broadened delithiation voltage plateau below 0.5 V. *J. Energy Chem.* **49**, 233–242 (2020).
48. Chen, J. et al. Electrolyte design for Li metal-free Li batteries. *Mater. Today* **39**, 118–126 (2020).
49. Zhang, H., Yang, Y., Ren, D., Wang, L. & He, X. Graphite as anode materials: fundamental mechanism, recent progress and advances. *Energy Storage Mater.* **36**, 147–170 (2021).
50. Cheng, F. et al. A 3D multifunctional host anode from commercial carbon cloth for lithium metal batteries. *J. Mater. Chem. A* **11**, 4205–4219 (2023).
51. Lin, D. et al. Layered reduced graphene oxide with nanoscale interlayer gaps as a stable host for lithium metal anodes. *Nat. Nanotechnol.* **11**, 626–632 (2016).
52. Bieker, G., Winter, M. & Bieker, P. Electrochemical in situ investigations of SEI and dendrite formation on the lithium metal anode. *Phys. Chem. Chem. Phys.* **17**, 8670–8679 (2015).
53. Lee, W., Suzuki, S. & Miyayama, M. Lithium storage properties of graphene sheets derived from graphite oxides with different oxidation degree. *Ceram. Int.* **39**, S753–S756 (2013).
54. Kim, T.-H. et al. Enlarging the d-spacing of graphite and polarizing its surface charge for driving lithium ions fast. *J. Mater. Chem. A* **2**, 7600–7605 (2014).
55. Persson, K. et al. Lithium diffusion in graphitic carbon. *J. Phys. Chem. Lett.* **1**, 1176–1180 (2010).
56. Baba, T., Sodeyama, K., Kawamura, Y. & Tateyama, Y. Li-ion transport at the interface between a graphite anode and Li₂CO₃ solid electrolyte interphase: ab initio molecular dynamics study. *Phys. Chem. Chem. Phys.* **22**, 10764–10774 (2020).
57. Çakmakçı, N. et al. Lithium-embedded carbon nanotube/graphite composite anode for lithium metal battery. *J. Energy Storage* **89**, 111618 (2024).
58. Zhang, X. et al. Regulating Li uniform deposition by lithiophilic interlayer as Li-ion redistributor for highly stable lithium metal batteries. *Chem. Eng. J.* **436**, 134945 (2022).
59. Nikodimos, Y. et al. Multifunctional electrospun PVDF-HFP gel polymer electrolyte membrane suppresses dendrite growth in anode-free li metal battery. *Energy Storage Mater.* **61**, 102861 (2023).
60. Kim, J. H., Lee, S., Lee, J. W., Song, T. & Paik, U. 3D-interconnected nanoporous RGO-CNT structure for supercapacitors application. *Electrochim. Acta* **125**, 536–542 (2014).
61. Pei, S., Zhao, J., Du, J., Ren, W. & Cheng, H.-M. Direct reduction of graphene oxide films into highly conductive and flexible graphene films by hydrohalic acids. *Carbon* **48**, 4466–4474 (2010).
62. Kresse, G. & Furthmüller, J. Efficient iterative schemes for ab initio total-energy calculations using a plane-wave basis set. *Phys. Rev. B* **54**, 11169–11186 (1996).
63. Blöchl, P. E. Projector augmented-wave method. *Phys. Rev. B* **50**, 17953–17979 (1994).
64. Perdew, J. P., Burke, K. & Ernzerhof, M. Generalized gradient approximation made simple. *Phys. Rev. Lett.* **77**, 3865–3868 (1996).

Acknowledgements

S. Lee and S. Yang contributed equally to this work. This work was supported by the National Research Foundation of Korea (NRF) grant funded by the Korea government (MSIT) (RS-2025-02218301). This research was also supported by the Nano & Material Technology Development Program through the National Research Foundation of Korea (NRF) funded by Ministry of Science and ICT (No. RS-2024-00412289).

Author contributions

S.L. and S.Y. contributed equally to this work. S.L. and S.Y. designed and conducted the main experiments, analyzed the data, and were major contributors in writing the manuscript. M.S.K. supported materials synthesis and data acquisition. Y.B. assisted with electrochemical measurements and data interpretation. K.L., Y.J., and T.K. contributed to structural and morphological characterization and provided experimental resources. Y.H.K. and J.Y.K. supported material processing and contributed to characterization analysis. K.C.R. assisted with electrochemical evaluations and provided critical discussion. J.S. advised on data analysis and manuscript refinement. S.B.C. performed the D.F.T. calculations and contributed to theoretical interpretation. J.C. supervised the overall experimental design, provided instrumental support, and contributed to manuscript revision. T.K. provided resources and technical guidance for materials processing. P.J.K. supervised the entire project, coordinated the writing process, and finalized the manuscript. All authors read and approved the final manuscript.

Competing interests

The authors declare no competing interests.

Additional information

Supplementary information The online version contains supplementary material available at <https://doi.org/10.1038/s41528-025-00474-9>.

Correspondence and requests for materials should be addressed to Sung Beom Cho, Junghyun Choi, Taehoon Kim or Patrick Joohyun Kim.

Reprints and permissions information is available at <http://www.nature.com/reprints>

Publisher's note Springer Nature remains neutral with regard to jurisdictional claims in published maps and institutional affiliations.

Open Access This article is licensed under a Creative Commons Attribution-NonCommercial-NoDerivatives 4.0 International License, which permits any non-commercial use, sharing, distribution and reproduction in any medium or format, as long as you give appropriate credit to the original author(s) and the source, provide a link to the Creative Commons licence, and indicate if you modified the licensed material. You do not have permission under this licence to share adapted material derived from this article or parts of it. The images or other third party material in this article are included in the article's Creative Commons licence, unless indicated otherwise in a credit line to the material. If material is not included in the article's Creative Commons licence and your intended use is not permitted by statutory regulation or exceeds the permitted use, you will need to obtain permission directly from the copyright holder. To view a copy of this licence, visit <http://creativecommons.org/licenses/by-nc-nd/4.0/>.

© The Author(s) 2025